

Hygroscopic growth of atmospheric aerosol particles based on active remote sensing and radiosounding measurements: selected cases at Southeastern Spain

M. J. Granados-Muñoz^{1,2}, F. Navas-Guzmán^{1,2,*}, J. A. Bravo-Aranda^{1,2}, J. L. Guerrero-Rascado^{1,2}, H. Lyamani^{1,2}, A. Valenzuela^{1,2}, G. Titos^{1,2}, J. Fernández-Gálvez^{1,2}, and L. Alados-Arboledas^{1,2}

1 Dpt. Applied Physics, Faculty of Sciences, University of Granada, Fuentenueva s/n, 18071, Granada, Spain

2 Andalusian Institute for Earth System Research (IISTA-CEAMA), Avda. del Mediterráneo s/n, 18006, Granada, Spain

* Now at Institute of Applied Physics (IAP), University of Bern, Bern, Switzerland

Corresponding author: María José Granados Muñoz. Departamento de Física Aplicada, Universidad de Granada, Granada, Spain.

Phone: +34 958241000 (31174)

E-mail: mjgranados@ugr.es

Key words: hygroscopic growth, lidar, EARLINET, LIRIC, radiosounding

1 **Abstract**

2 A new methodology based on combining active and passive remote sensing and
3 simultaneous and collocated radiosounding data to study the aerosol hygroscopic growth
4 effects on the particle optical and microphysical properties is presented. The identification
5 of hygroscopic growth situations combines the analysis of multispectral aerosol particle
6 backscatter coefficient and particle linear depolarization ratio with thermodynamic
7 profiling of the atmospheric column. We analysed the hygroscopic growth effects on
8 aerosol properties, namely the aerosol particle backscatter coefficient and the volume
9 concentration profiles, using data gathered at Granada EARLINET station. Two study
10 **cases**, corresponding to different aerosol loads and different aerosol types, are used for
11 illustrating the potential of this methodology. Values of the aerosol particle backscatter
12 coefficient enhancement factors range from 2.1 ± 0.8 to 3.9 ± 1.5 , in the ranges of relative
13 **humidity 60-90% and 40-83%**, being similar to those previously reported in the literature.
14 Differences in the enhancement factor are directly linked to the composition of the
15 atmospheric aerosol. The largest value of the aerosol particle backscatter coefficient
16 enhancement factor corresponds to the presence of sulphate and marine particles that are
17 more affected by hygroscopic growth. On the contrary, the lowest value of the
18 enhancement factor corresponds to an aerosol mixture containing sulphates and slight
19 traces of mineral dust. The Hänel parameterization is applied to these case studies,
20 obtaining results within the range of values reported in previous studies, with values of the
21 γ exponent of 0.56 ± 0.01 (for anthropogenic particles slightly influenced by mineral dust)
22 and 1.07 ± 0.01 (for the situation dominated by anthropogenic particles), showing the
23 convenience of this remote sensing approach for the study of hygroscopic effects of the
24 atmospheric aerosol under ambient unperturbed conditions. For the first time, the retrieval
25 of the volume concentration profiles for these cases using the Lidar Radiometer Inversion
26 Code (LIRIC) allows us to analyse the aerosol hygroscopic growth effects on aerosol
27 volume concentration, observing a stronger increase of the fine mode volume concentration
28 with increasing relative humidity.

29 **1. INTRODUCTION**

30 The influence of atmospheric aerosols in the Earth's climate is still affected by a high
31 uncertainty. Scientific knowledge on the interaction between atmospheric aerosol and solar
32 radiation is quite low compared to other atmospheric constituents mainly due to
33 atmospheric aerosol high spatio-temporal variability [IPCC, 2013]. As it is well known,
34 atmospheric aerosol can affect the Earth-Atmosphere energy budget by means of direct
35 effects (by scattering or absorbing solar radiation) and indirect effects (mainly by changes
36 in cloud properties). Therefore, changes in aerosol properties can highly influence the
37 Earth's climate. Aerosol particles size may increase due to water uptake (hygroscopic
38 growth) altering their size distribution and their associated optical and microphysical
39 properties under high relative humidity conditions. Therefore, hygroscopic growth affects
40 the direct scattering of radiation [Hänel, 1976; Hegg *et al.*, 1996; Titos *et al.*, 2014; Zieger
41 *et al.*, 2014] and especially the indirect effects, as the affinity of atmospheric aerosols for
42 water vapor is highly related to their ability to act as cloud condensation nuclei (CCN)
43 [Charlson *et al.*, 1992; Feingold and Morley, 2003; Padró *et al.*, 2010].

44 In the past years there has been an increasing interest in the hygroscopic growth
45 effects on the aerosol optical and microphysical properties and many studies have already
46 been performed [e. g. Veselovskii *et al.*, 2009; Zieger *et al.*, 2013; Titos *et al.*, 2014a,
47 2014c]. Much of the recent research was performed by means of humidified nephelometers
48 [Covert *et al.*, 1972; Fierz-Schmidhauser *et al.*, 2010a, and references therein] or
49 humidified tandem differential mobility analysers [Massling *et al.*, 2007; Wu *et al.*, 2013,
50 and references therein]. Nonetheless, these instruments present two main problems. Firstly,
51 due to experimental set-up limitations it is difficult to provide accurate results above RH of
52 85% [Wulfmeyer and Feingold, 2000]. Secondly, they modify the ambient conditions by
53 drying the air sample and then humidifying it again up to a certain value of RH, altering
54 thus the aerosol properties and being also subject to aerosol losses in the sampling lines.

55 Opposite to in-situ measurements, lidar systems present as main advantage that they
56 can provide vertically resolved measurements without modifying the aerosol sample or its
57 surroundings. They also detect RH close to saturation, which is of great importance since
58 the range between 85 and 100% RH is where the particles are more affected by hygroscopic
59 growth [Feingold and Morley, 2003]. Therefore, they are adequate to provide useful
60 information about aerosol hygroscopic properties if favourable atmospheric conditions

61 occur. However, they present the major drawback that the sample and conditions are not
62 controlled in anyway and the number of cases with adequate conditions is usually low
63 compared to in-situ measurements. In the past years, some studies have already been
64 performed by using lidar systems to detect aerosol hygroscopic growth with promising
65 results [Ferrare et al., 1998; Wulfmeyer and Feingold, 2000; Feingold and Morley, 2003;
66 Veselovskii et al., 2009; DiGirolamo et al., 2013]. However, many of these studies present
67 the major drawback that experimental RH profiles were not available and assumptions were
68 made to obtain RH data [Wulfmeyer and Feingold, 2000; Feingold and Morley, 2003;
69 Feingold et al., 2006; Pahlow et al., 2006]. In some other cases, RH profiles were taken
70 from quite distant radiosounding measurements [Veselovskii et al., 2009]. The availability
71 of collocated radiosounding data allows the reduction of assumptions needed. In this study,
72 a methodology to study aerosol hygroscopic growth based on lidar data and collocated
73 radiosounding RH profiles is presented and applied at Granada EARLINET (European
74 Aerosol Research Lidar Network) experimental site in order to study aerosol hygroscopic
75 growth under unperturbed ambient conditions.

76 2. EXPERIMENTAL SITE AND INSTRUMENTATION

77 This study was performed at the Andalusian Institute for Earth System Research,
78 IISTA-CEAMA, located in Granada (37.16° N, 3.61° W, 680 m a.s.l.). The station is
79 described in more detail in [Lyamani et al., 2010; Titos et al., 2012; Valenzuela et al.,
80 2012]. Granada is affected by continental climate conditions. Temperature presents large
81 seasonal variations, with cool winters and hot summers, and a strong diurnal thermal
82 oscillation (up to 20 °C), which lead to strong RH variations along the day. Seasonal
83 variations in RH are also quite important with mean monthly values ranging between 41%
84 in summer and 76% in winter (source: State Meteorological Agency, www.aemet.es). An
85 analysis of RH profiles based on measurements of water vapour mixing ratio from Raman
86 lidar and temperature from microwave radiometry for one-year period, performed for
87 500m-layers at different altitudes revealed that over Granada the 60% of the data present
88 RH values in the range between 20 and 60%, whereas only 25% of these layers present
89 values larger than 60% [Navas-Guzmán et al., 2014].

90 Due to its proximity to the African continent, the experimental site is usually affected
91 by mineral dust events [Valenzuela et al., 2012], reaching altitudes of up to 5500 m a.s.l.

92 [Guerrero-Rascado et al., 2008; 2009; Navas-Guzmán et al., 2013]. In addition, Europe acts
93 as an important source of anthropogenic pollution [Lyamani et al., 2006a,b]. The
94 experimental site is also affected by local and regional sources. In a recent source
95 apportionment study of fine and coarse particulate matter at surface level, Titos et al.
96 [2014b] pointed out that the major aerosol sources at Granada are road traffic (dominated
97 by diesel engines) and mineral dust as well as fuel-based domestic heating during winter
98 time. The levels of mineral matter increase considerably from winter to summer due to the
99 dryness conditions, which favour re-suspension processes and the higher frequency of
100 Saharan outbreaks. Traffic related sources increase its contribution during winter compared
101 with summer [Titos et al., 2014b] as a consequence of higher emissions and lower mixing
102 layer heights [Granados-Muñoz et al., 2012].

103 The experimental station is equipped with a multiwavelength Raman lidar system
104 model LR331D400 (Raymetrics S.A.). Such instrument, called MULHACEN, is described
105 in detail in Guerrero-Rascado et al., [2008, 2009]. The lidar system emits at 355, 532 and
106 1064 nm. The detection system records the elastic signals at these three wavelengths and
107 Raman signals in three additional channels: 387 and 607 nm, corresponding to the nitrogen
108 Raman channel, and 408 nm, corresponding to water vapour Raman channel. In addition,
109 the perpendicular and parallel components of the visible channel are detected, allowing us
110 to study the depolarization properties of the atmospheric aerosol [Bravo-Aranda et al., 2013
111 and references therein]. Uncertainties associated to the elastic lidar signals are around 15%,
112 considering the statistical uncertainties retrieved with Monte Carlo techniques according to
113 Pappalardo et al., [2004] and Guerrero-Rascado et al., [2008]. The Raman lidar is part of
114 EARLINET [Pappalardo et al., 2014]. It has been part of the EARLINET-ASOS (European
115 Aerosol Research Lidar Network - Advanced Sustainable Observation System) project and
116 currently is included in the ACTRIS (Aerosols, Clouds, and Trace gases Research
117 InfraStructure Network) European project.

118 In addition, the radiometric station is equipped with a sun photometer CIMEL CE-318-4.
119 The sun photometer provides column-integrated atmospheric aerosol properties. The
120 automatic tracking sun and sky scanning radiometer makes sun direct measurements with a
121 1.2° full field of view every 15 min at 340, 380, 440, 500, 675, 870, 940 and 1020 nm
122 (nominal wavelengths). These solar extinction measurements are used to compute aerosol

123 optical depth (τ_λ) at each wavelength except for the 940 nm channel, which is used to
124 retrieve total column water vapour (or precipitable water). The estimated uncertainty in
125 computed τ_λ , due primarily to calibration uncertainty, is around 0.010–0.021 for field
126 instruments (which is spectrally dependent, with the higher errors in the UV) [Eck et al.,
127 1999]. The sun photometer located in Granada is included in the AERONET network
128 [Holben et al., 1998]. Uncertainty of AERONET inversion products is described in detail in
129 Dubovik et al. [2000]. The study showed that the uncertainty in the retrieved single
130 scattering albedo, $\omega(\lambda)$, is ± 0.03 for high aerosol load ($\tau_{440\text{nm}} > 0.4$) and solar zenith angle
131 $\theta > 50^\circ$. In cases with low aerosol load ($\tau_{440\text{nm}} < 0.2$), the retrieval accuracy of $\omega(\lambda)$, drops
132 down to 0.02-0.07 [Dubovik et al., 2000]. For $\tau_{440\text{nm}} > 0.4$ and $\theta > 50^\circ$ the imaginary part
133 of the refractive index is about 20-50%. The aerosol size distribution retrieval depends on
134 aerosol particle sizes, types and actual values of the size distribution. For particles in the
135 size range $0.1 < r < 7 \mu\text{m}$, the uncertainty is around 10-35%, whereas for sizes lower than 1
136 μm and higher than 7 μm the uncertainty increases up to 80-100%. The AERONET Version
137 2 Level 1.5 data are used in this study for the characterization of the aerosol properties and
138 for the retrieval of the aerosol microphysical properties profiles in combination with
139 backscattered elastic lidar signals by means of the Lidar Radiometer Inversion Code
140 (LIRIC) [Chaikovsky et al., 2012; Wagner et al., 2013; Granados-Muñoz et al., 2014].

141 For the analysis of the aerosol hygroscopic properties at the station, specific
142 radiosounding launch campaigns are performed in order to obtain the RH humidity profiles
143 since 2011. Radiosoundings (DFM-09 from GRAW Radiosondes) are launched
144 simultaneously and collocated to the lidar measurements. They provide temperature
145 (resolution 0.01°C, accuracy 0.2°C), pressure (resolution 0.1 hPa, accuracy 0.5 hPa),
146 humidity (resolution 1%, accuracy 2%) and wind speed (resolution 0.1 m/s, accuracy 0.2
147 m/s) profiles. Data acquisition and processing are performed by Grawmet5 software and a
148 GS-E ground station from the same manufacturer. GRAW Radiosondes showed good
149 performance at previous intercomparison studies, especially for the RH in the lower
150 troposphere (deviations below 2%) [Sun et al., 2013].

151 In addition, analysis of backwards trajectories is performed in this study by means of
152 the HYSPLIT model (HYbrid Single-Particle Lagrangian Integrated Trajectory) [Draxler
153 and Rolph, 2003]. 5-day backwards trajectories of air masses arriving at the experimental

154 site at different height levels depending on the region of interest are computed using the
155 model including vertical wind information. The trajectories analysis allows the
156 interpretation of the source regions of air masses reaching the experimental site. Under low
157 wind conditions, trajectories can have relative error $\sim 40\%$ [Stunder, 1996]. The Global
158 Data Assimilation System (GDAS) database is used as input meteorological database for
159 the computations.

160 3. METHODOLOGY

161 3.1. Retrieval of aerosol optical and microphysical properties and relative humidity 162 profiles

163 From the inversion of the lidar data, the aerosol particle backscatter coefficient profiles
164 (β^P_λ) are obtained by applying the Klett-Fernald inversion algorithm [Fernald, 1984;
165 Fernald et al., 1972; Klett, 1981, 1985]. This algorithm assumes a reference height free of
166 aerosol particles and a height independent aerosol particle lidar ratio (extinction-to-
167 backscatter ratio) for each wavelength. More details can be found in [Bravo-Aranda et al.,
168 2013 and references therein] and [Guerrero-Rascado et al., 2009; 2011]. Aerosol particle
169 lidar ratios assumed when applying the Klett-Fernald algorithm to the lidar data are
170 obtained by minimizing the difference between the integral of the aerosol particle
171 backscatter coefficient profile multiplied by the particle lidar ratio and the aerosol optical
172 depth provided by AERONET for each wavelength [Guerrero-Rascado et al., 2008;
173 Landulfo et al., 2003]. The aerosol particle backscatter related Angström exponent profiles
174 between 355 and 532 nm (β -AE(355-532nm)), related to the aerosol particles size, are also
175 obtained. In addition, the particle linear depolarization ratio profiles ($\delta^P_{532\text{nm}}$) are also
176 calculated as explained in [Bravo-Aranda et al., 2013] in order to analyse variations in the
177 shape of the particles. The assumption of a height-independent lidar ratio in Klett retrieval
178 might be a source of error in cases of non-homogenous aerosol layers, but even incorrect
179 assumed backscatter-to-extinction ratios can yield rather accurate results [Kovalev, 1995].
180 In general, the errors in the profiles obtained with the Klett method are less than 20% for
181 β^P_λ and less than 25% for $\delta^P_{532\text{nm}}$ [Franke et al., 2001; Alados-Arboledas et al., 2011;
182 Preissler et al., 2011].

183 The volume concentration profiles are retrieved by means of Lidar Radiometer Inversion
184 Code (LIRIC) [Chaikovsky et al., 2012]. This algorithm provides vertical profiles of

185 microphysical properties from a combined set of sun photometer and lidar data. LIRIC
186 inputs are column-integrated optical and microphysical properties retrieved from the sun
187 photometer measurements using AERONET code [Dubovik et al., 2006] and measured
188 lidar elastic backscatter signals at three different wavelengths (355, 532, and 1064nm). The
189 depolarization information from lidar data can be optionally used. From AERONET code,
190 input variables used by LIRIC are columnar integrated volume concentration values for
191 each mode, refractive index, single scattering albedo, integrated backscatter coefficients,
192 the first and second diagonal elements of the scattering matrices at 180°, the fraction of the
193 spherical particles and the aerosol optical depth. In addition, based also on AERONET
194 code, an aerosol model, defined by the columnar integrated volume concentrations of each
195 mode (fine and coarse modes) and based on a mixture of randomly oriented spherical and
196 spheroid particles, is assumed [Dubovik and King, 2000; Dubovik et al., 2006]. These data,
197 together with the elastic lidar raw signals at 355, 532 and 1064 nm, are used to obtain the
198 volume concentration profiles for fine and coarse particles, distinguishing between coarse
199 spherical and coarse spheroid mode when 532-nm cross-polarized lidar channel is used.
200 The mathematical procedure used to retrieve the volume concentration profiles is described
201 in detail in Chaikovsky et al., [2008.]. It is worthy to point out here that the refractive
202 index, percentage of sphericity and size distribution for each mode are assumed as height-
203 independent in LIRIC retrievals. In cases of different aerosol types in the atmospheric
204 column or variation of these properties with height, this assumption may introduce some
205 uncertainties. Therefore, it is necessary to consider the limitations of LIRIC under these
206 specific situations when analysing LIRIC results. Ancillary information, such as the lidar
207 retrieved optical properties profiles, has to be used in order to guarantee the reliability of
208 the results. In cases of hygroscopic growth, it is clear that the refractive index is height-
209 dependent, since it varies with increasing/decreasing relative humidity due to the changes
210 in the aerosol composition. However, we performed some tests with LIRIC by varying the
211 refractive index provided by AERONET, which is the one used by LIRIC, and keeping all
212 the other parameters in LIRIC code unvaried. The volume concentration profiles retrieved
213 for the different values of refractive index were almost the same (with differences below
214 7.5%). Therefore, it can be assumed that LIRIC's sensitivity to variations of the refractive
215 index is very low and the associated uncertainty is quite small.

216 The RH profiles are directly measured by the radiosounding simultaneously and
217 collocated to the lidar measurements, therefore no assumptions concerning the RH profile
218 are needed as in previous studies [Ferrare et al., 1998; Wulfmeyer and Feingold, 2000;
219 Feingold and Morley, 2003].

220 3.2.Procedure for selection of hygroscopic growth case studies

221 For the retrieval of the aerosol hygroscopic properties from lidar data, very specific
222 conditions need to be fulfilled. Aerosol water uptake is associated to the increase in aerosol
223 optical properties such as the aerosol particle backscatter coefficient β_{λ}^P and aerosol particle
224 microphysical properties such as the volume concentration. Therefore, for the study of
225 these hygroscopic properties, we need to observe an increase in the aerosol particle
226 backscatter at a certain aerosol layer. This increase has to occur simultaneously to an
227 increase in RH in this aerosol layer in order to consider hygroscopic growth as the possible
228 cause of the changes in the aerosol particles properties. Those cases fulfilling the previously
229 described conditions are considered as potential cases of hygroscopic growth.

230 β -AE and δ_{532nm}^P profiles are analysed as ancillary information. In general, a
231 simultaneous decrease of these two properties is indicative of larger and more spherical
232 particles, which is a good indicator of aerosol hygroscopic growth. This positive correlation
233 between these two aerosol properties usually occur only in cases of aerosol hygroscopic
234 growth or aging processes. Nonetheless, during our analysis it was observed that the
235 decrease in the β -AE, even though existing, is quite smooth and variations are within the
236 uncertainty limits. Therefore, a more detailed analysis with more case studies and based on
237 Raman analysis will be needed to reinforce this conclusion.

238 Once the potential cases of hygroscopic growth are detected, it is necessary to verify
239 that in the analysed aerosol layer the atmospheric aerosol particles present a certain degree
240 of homogeneity. In this way, we can corroborate that the variations in the aerosol particle
241 properties such as β_{λ}^P and the volume concentration, are caused by the increase in the
242 aerosol size due to water uptake and not to changes in the aerosol composition or load in
243 the analysed layer. That means that the same aerosol type or mixture must be present along
244 the analysed height range and almost no variations in the aerosol load must exist. For this
245 purpose, ancillary information such as the backward trajectories of the air masses, the

246 profiles of potential temperature, θ , or the water vapour mixing ratio profiles, r , are used to
 247 ensure that the aerosol layer under study is affected by hygroscopic growth. In this sense, if
 248 the origin and the trajectory of the air masses are independent of the altitude in the layer
 249 analysed, it is considered that the same aerosol type might have been advected and,
 250 therefore, a homogenous aerosol composition might be expected in the analysed layer.
 251 Otherwise, variations in the aerosol composition are expected and the case is not considered
 252 for analysis of hygroscopic growth. These **air mass** backward trajectories analyses are
 253 mainly used as a first approach selection criterion. In addition, good mixing is required as a
 254 boundary condition in order to guarantee the homogeneity of the atmospheric aerosol in the
 255 investigated layer. In general, constant profiles of θ and r are indicators of well mixed
 256 conditions within the atmosphere. In our analysis, θ and r are calculated in the analysed
 257 layer to check the mixing conditions. Both atmospheric variables are calculated from the
 258 radiosounding temperature and relative humidity profiles. Only those cases with almost
 259 constant values of θ and r in the analysed layer (variations lower than 2° and 2 g/kg
 260 respectively) will be consider for the analysis. Good mixed conditions cannot be guaranteed
 261 in any other case.

262 The backward trajectories analysis and the height independency of r criteria for
 263 identifying hygroscopic growth were already used in the study by Veselovskii et al., [2009].
 264 However, the height independency of θ is introduced for the first time in this study in order
 265 to provide more robust boundary conditions and guarantee the occurrence of hygroscopic
 266 growth **within a well-mixed layer** [Stull, 1988].

267 If these requirements for the homogeneity on the atmospheric aerosol layer are
 268 fulfilled, these cases are selected for a more detailed analysis of atmospheric aerosol
 269 hygroscopic properties. For the analysis of the hygroscopic growth, the enhancement factor
 270 is defined as:

$$f_{\zeta}(RH) = \frac{\zeta(RH)}{\zeta(RH_{ref})} \quad \text{Eq. 1}$$

271 where $\zeta(RH)$ represents an aerosol property at a certain RH. RH_{ref} is the so-called reference
 272 RH. This RH_{ref} is chosen as the lowest value of RH in the analysed layer. For this study,
 273 $f_{\zeta}(RH)$ is obtained for β_{λ}^P profiles ($f_{\beta}(RH)$) and the volume concentration profiles ($f_{VC}(RH)$).

274 The enhancement factor total uncertainty is very difficult to determine since it is
275 highly dependent on the uncertainties of the aerosol properties and the RH, **the uncertainty**
276 **in the vertical and temporal coordinates**, on the range of RH considered as well as the
277 hygroscopic growth of the particle itself and therefore it is not well characterized yet. **There**
278 **is still a lack of studies about the characterization of the enhancement factor uncertainty**
279 **that should be fulfilled in future studies.** Adam et al., [2012] provided estimations based on
280 a sensitivity test and Mie calculations. According to their study, this uncertainty varies
281 between 4% (for RH < 40%) and 38% (at RH > 95%).

282 For different cases, the ranges of RH and, as a consequence, RH_{ref} values are
283 different. Therefore, in order to make the different results comparable it is necessary to use
284 a common RH_{ref} value. For this purpose, the Hänel model [Hänel, 1976] is used to
285 parameterize the experimental enhancement factor curves. The general form of the Hänel
286 equation is expressed as:

$$f_{\zeta}(\text{RH}) = \left(\frac{1 - \text{RH}}{1 - \text{RH}_{\text{ref}}} \right)^{-\gamma} \quad \text{Eq. 2}$$

287 where γ is an indicator of the hygroscopicity of the particles. Larger γ values are related to
288 more hygroscopic aerosol types.

289 Since atmospheric aerosol hygroscopic properties are highly dependent on the aerosol
290 chemical composition information, NAAPS (Navy Aerosol Analysis and Prediction
291 System) [Christensen, 1997] model is also considered in this study to support the data
292 interpretation with respect to the aerosol type.

293 Summarizing, for the detection of aerosol hygroscopic growth the following
294 procedure is followed: 1) Detection of the aerosol particle backscatter coefficient increase
295 with simultaneous increase in RH in a certain aerosol layer, 2) Confirmation that the
296 atmospheric aerosol layer under study is homogenous. For this purpose, **homogeneity**
297 boundary conditions are implemented: the origin and the trajectory of the air masses at the
298 analysed layer has to be independent of the altitude and the profiles of r and θ has to be
299 constant with height in this layer as an indicative of well mixed conditions.

300 4. RESULTS AND DISCUSSION

301 Data corresponding to several radiosounding launch campaigns performed at the
302 experimental site during the period 2011 to 2013 were analysed following the methodology
303 described in the previous section. During this period, lidar measurements were always
304 running in coincidence with the radiosounding launches. These lidar measurements have
305 been exhaustively analysed together with the RH profiles provided by the radiosoundings
306 in order to detect cases of aerosol hygroscopic growth. Two case studies corresponding to
307 22nd July 2011 and 22nd July 2013 are presented here to show the potential of the technique
308 described in section 3.2. In these case studies, atmospheric conditions are highly supportive
309 for aerosol hygroscopic growth at certain height ranges. A detailed analysis of these cases
310 is presented in the following paragraphs.

311 Case I corresponds to the 22nd July 2011. On this day, a radiosounding was launched
312 at 20:30 UTC in coincidence with night-time lidar measurements. According to NAAPS
313 model, 22nd July 2011 at 18:00 UTC is characterized by the presence of mineral dust above
314 Granada (Figure S1a from Supplementary material). **However, this is not in agreement with**
315 **the experimental data at the time of the measurements. Mineral dust was observed just as a**
316 **remaining small layer at high altitude from a previous dust event above the station, but it**
317 **was not the predominant aerosol type. No presence of mineral dust was detected in the**
318 **aerosol layer studied for hygroscopic growth, as we will show later on.** A second case of
319 hygroscopic growth is detected on 22nd July 2013 (Case II) during the summer
320 radiosounding campaign. For this specific day, the radiosounding was launched at 20:00
321 UTC in coincidence with simultaneous lidar measurements. On this day, NAAPS model
322 indicates the presence of sulphates and smoke above the experimental site (Figure S1b).

323 [Figure S1]

324 Sun photometer experimental data are also used for this analysis, since they provide
325 information about the aerosol properties. In addition, sun photometer data are required for
326 the retrieval of the volume concentration profiles with LIRIC. For Case I, sun photometer
327 data suggest the presence of a Saharan dust plume that dissipates at late afternoon (Figure
328 1a), **when our measurements took place.** The aerosol optical depth at 440 nm ($\tau_{440\text{nm}}$)
329 decreases during the afternoon, changing from 0.30 in the morning to values of 0.20 at
330 18:30 UTC. The Angström exponent between 440 and 870 nm (AE(440-870nm)) increases
331 from 0.5 to 1.1, indicating an enhancement in the contribution of fine particles from 15:00

332 UTC. The aerosol size distributions retrieved during the day also indicate a decrease in the
333 coarse mode and an increase of the fine mode from midday onwards. At 18:30 UTC (Figure
334 1b) the aerosol size distributions indicate a balanced presence of both fine and coarse
335 particles. This is confirmed by the fine mode fraction, determined through the SDA
336 (spectral deconvolution algorithm, not shown) [O'Neill et al., 2003] that increases from
337 0.35 in the early morning up to 0.55 in the late evening. In the retrievals of single scattering
338 albedo, $\omega(\lambda)$, corresponding to the morning hours it is observed a strong influence of
339 mineral dust (high $\omega(\lambda)$ values and increasing $\omega(\lambda)$ with wavelength) (Figure 1c). However,
340 in the late afternoon, $\omega(\lambda)$ values around 0.93, and its neutral spectral dependence suggest
341 the presence in the atmospheric column of aerosol from anthropogenic origin with
342 influence of residual mineral dust [Lyamani et al., 2006; Valenzuela et al., 2012], which
343 will be confirmed later with the lidar data and the backward trajectories analysis (Figure
344 1c).

345 For the second case, $\tau_{440\text{nm}}$ values indicate high aerosol loads reaching values above
346 0.40 at 17:19 UTC (Figure 1d). The AE(440-870nm) exhibits values larger than 1.2 during
347 the whole day reaching 1.4 at 18:30 UTC, thus indicating a predominance of fine particles.
348 The AERONET inversion retrievals during the whole day show bimodal size distributions
349 with predominance of fine particles mode (Figure 1e). Both, the $\omega(440\text{ nm})$ values close to
350 0.9, and their spectral dependence, with a decreasing trend with wavelength, evidence the
351 presence of anthropogenic pollution and/or smoke over Granada [Lyamani et al., 2006]
352 (Figure 1f), in agreement with NAAPS forecast model.

353 [Figure 1]

354
355 On both case studies, lidar measurements were running from 20:00 to 22:00 UTC. On
356 22 July 2011, lidar range corrected signal (RCS) time series (Figure 2a) indicate the
357 presence of atmospheric aerosol up to 3000 m a.s.l. Moreover, a strong increase of the RCS
358 is observed inside the height range around 2400 m a.s.l. between 20:30 and 21:00 UTC. On
359 the other hand, the time series of the lidar RCS on 22 July 2013 (Figure 2b) indicate that
360 the atmospheric aerosol reach altitudes up to 3500 m a.s.l. with the strongest backscattered
361 lidar signal around 3000 m a.s.l. For this second case, some clouds were observed from

362 21:30 UTC. The occurrence of these clouds might be related to the ability of hygroscopic
363 aerosol to act as CCN.

364 [Figure 2]

365 The analysis of lidar data by means of the Klett-Fernald inversion algorithm for both
366 cases is shown in Figure 3. Mean profiles of $\beta_{532\text{nm}}^{\text{P}}$, $\beta\text{-AE}(355\text{-}532\text{nm})$ and $\delta_{532\text{nm}}^{\text{P}}$
367 corresponding to the period from 20:30 to 21:00 UTC for Case I and to 20:00- 20:30 UTC
368 for Case II are presented in this figure. On both cases, we observe a marked increase with
369 altitude in $\beta_{532\text{nm}}^{\text{P}}$ in the range between 1330 and 2330 m a.s.l. for Case I and 1300 and
370 2700 m a.s.l. for Case II (Figure 3a). Simultaneous to this increase in $\beta_{532\text{nm}}^{\text{P}}$, the RH also
371 increase with altitude in both layers (Figure 3b). Water vapour mixing ratio, r , profiles
372 retrieved from the radiosounding data are shown in figure 3c. Opposite to $\beta_{532\text{nm}}^{\text{P}}$, $\beta\text{-}$
373 AE(355-532nm) decreases with altitude in the both layers (Figure 3d, Table 1). The
374 decrease in $\beta\text{-AE}(355\text{-}532\text{nm})$ with altitude indicates an increase in aerosol particles size at
375 higher altitudes, even though it is necessary to be aware that the decrease is very smooth
376 and the variations are within the uncertainty limits in both cases. The $\delta_{532\text{nm}}^{\text{P}}$ also decreases
377 with altitude for both cases in the corresponding aerosol layers (Figure 3e). The decrease in
378 $\delta_{532\text{nm}}^{\text{P}}$ is stronger than the one observed in $\beta\text{-AE}(355\text{-}532\text{nm})$ and it indicates that there is
379 an increase in particle sphericity, which is a typical behaviour of hygroscopic growth. The
380 observed positive correlation between $\beta\text{-AE}(355\text{-}532\text{nm})$ and $\delta_{532\text{nm}}^{\text{P}}$ might be a very good
381 indicator of aerosol hygroscopic growth and, up to our knowledge, it has never been
382 presented in previous studies. However, due to the uncertainty in $\beta\text{-AE}(355\text{-}532\text{nm})$, it has
383 to be carefully read in this particular study and a more comprehensive study with more case
384 studies will be necessary, as previously stated. On Case I, $\delta_{532\text{nm}}^{\text{P}}$ profiles retrieved from
385 lidar data in the analysed aerosol layer are rather low ($\delta_{532\text{nm}}^{\text{P}} \sim 0.07$), indicating
386 predominance of spherical particles in the analysed layer. However, at higher altitudes
387 $\delta_{532\text{nm}}^{\text{P}}$ reach values of 0.15 and $\beta\text{-AE}(355\text{-}532\text{nm}) \sim 0.6$ with RH values lower than 40%,
388 indicating that the influence of mineral dust observed in the column with the sun
389 photometer data is more important in this upper layer than in our region of interest.

390 [Table 1]

391 [Figure 3]

392 [Figure 4]

393

394 In order to corroborate that the variations with height in the aerosol properties are due
395 to water uptake and not to inhomogeneities in the aerosol layer, the boundary conditions
396 established in section 3.2 are checked (Figure 4). The 5-day backward trajectories analysis
397 performed with HYSPLIT model reveals that the origin and trajectories of the air masses
398 are almost identical for the different altitudes within the aerosol layer considered in each
399 case. Therefore, the same aerosol type might have been advected over Granada in the
400 investigated aerosol layers. For Case I, air masses come from the Northwest of Europe,
401 going through the Northern Iberian Peninsula, finally arriving over Granada after
402 overpassing the Iberian Peninsula Mediterranean Coast (Figure 4a). These air masses might
403 have transported anthropogenic aerosol from Europe to the experimental site, especially
404 considering that they were travelling at very low altitudes, located within the planetary
405 boundary layer according to HYSPLIT retrieved boundary layer heights. The backward
406 trajectories analysis also revealed that the air masses were travelling very close to the sea
407 surface above the Mediterranean Sea and marine aerosols might be probably present in the
408 aerosol mixture (Figure 4a). For Case II, the air masses come from the Mediterranean
409 region at the three altitude levels considered (Figure 4b) and they were travelling within the
410 marine boundary layer before reaching Granada station, so they are likely loaded with
411 marine aerosol from the Western Mediterranean Sea together with sulphates and smoke
412 from Europe as indicated by the NAAPS model. The trajectories are very similar to those
413 on Case I, but as for this case they travelled more slowly above the Mediterranean Sea they
414 are likely loaded with more marine aerosol than in the previous case.

415 Vertical profiles of θ and r measured with radiosounding data are also checked in
416 order to corroborate good mixing conditions within the analysed aerosol layers. Both θ and
417 r profiles present almost constant values in the analysed layers in both case studies (Figure
418 4c) and thus it can be inferred that the analysed layers are well mixed in both cases. Once
419 these conditions are fulfilled, vertical homogeneity in the analysed layers can be assumed.
420 Therefore, hygroscopic growth is foreseen for these cases since there is a high likelihood
421 that changes in the aerosol properties are due to water uptake.

422 Therefore, according to all the previous results, these cases are considered
423 representative of hygroscopic growth since there is an enhancement in $\beta_{532\text{nm}}^P$ in

424 coincidence with an increase in RH in the selected aerosol layers. In addition, the positive
425 correlation between the β -AE(355-532nm) and the δ^P_{532nm} values suggests hygroscopic
426 growth, since aerosol particles become larger and more spherical due to water uptake.
427 Backward trajectories analysis with HYSPLIT and the height independency of θ and r in
428 the analysed height range corroborates that the enhancement of β^{aer}_{532nm} is due to water
429 uptake because of the homogeneity of the aerosol layer.

430 Following the methodology described in Section 3.2, from the combination of the
431 β^P_{532nm} and RH profiles in Figure 3, the aerosol particle backscatter coefficient
432 enhancement factor $f_{\beta}(RH)$ is obtained as indicated in Eq.1.

433 In Case I, $RH_{ref}=60\%$, which is the lowest value measured in the investigated layer.
434 The dependence of $f_{\beta}(RH)$ with the RH is shown in the resultant humidogram in Figure 5a.
435 From this figure, it is evident that β^P_{532nm} increases 2.5 times ($f_{\beta}(90\%) = 2.5$) in the range of
436 humidity between 60 and 90% . The humidogram in Case II shows that $f_{\beta}(83\%) = 3.5$, in
437 the range of RH between 40 and 83%. For Case II, RH_{ref} is established at 40%, since it is
438 the lowest RH value reached in the analysed layer for this case.

439 [Figure 5]

440
441 In a similar study performed by Veselovskii et al. [2009] in the East Coast of the
442 United States, they got a value of the aerosol particle extinction coefficient enhancement
443 factor, $f_{\alpha}(85\%) = 2.3$ in the presence of the typical continental haze using $RH_{ref} = 60\%$. It is
444 necessary to take into account that Veselovskii et al. [2009] used the aerosol particle
445 extinction coefficient profile and thus results are comparable only in a contextual way, since
446 it would be necessary to know the influence of the aerosol hygroscopic growth on the
447 aerosol particle lidar ratio to perform a quantitative comparison. For Case I, the value
448 obtained here for $f_{\beta}(85\%)$ is much lower than the one provided by Veselovskii et al. [2009]
449 ($f_{\beta}(85\%) = 1.5$). However, for Case II $f_{\beta}(85\%) = 2.6$ using $RH_{ref} = 60\%$, which is very
450 similar to the one obtained by Veselovskii et al. [2009].

451 A qualitative comparison with in-situ studies can be done in order to contextualize
452 our results. However, when making this comparison it is necessary to take into account the
453 differences between both techniques. In addition, in-situ analyses are usually performed

454 under controlled conditions, whereas lidar data are measured under real and unperturbed
455 conditions. In addition, in-situ studies are frequently based on the retrieval of the aerosol
456 particle light-scattering coefficient enhancement factor $f_{\sigma}(RH)$ and not on the $f_{\beta}(RH)$ used
457 here. They usually provide values for $f_{\sigma}(85\%)$ using RH_{ref} values of 40% or lower (dry
458 conditions). In order to compare our results to these in-situ studies using a RH_{ref} of 40%,
459 the Hänel parameterization is applied to our data in Case I (Figure 5a). For Case II, the
460 Hänel parameterization is necessary to obtain $f_{\beta}(85\%)$, since RH values above 83% are not
461 reached. Values of $f_{\beta}(80\%)$, $f_{\beta}(85\%)$ using $RH_{ref}=40\%$ and γ obtained are summarized for
462 both cases in Table 2.

463 [Table 2]

464 As it can be inferred from Table 2 and Figure 5, the atmospheric aerosol presents a
465 stronger hygroscopic growth for Case II. According to the experimental AERONET and
466 lidar data and the ancillary information of the model, this may be to the larger contribution
467 of sulphates (in the fine mode) and marine aerosol (in the coarse mode) during Case II than
468 during Case I in the analysed layers. In addition, a minor influence of the residual mineral
469 dust particles (which presents very low hygroscopicity) from the morning hours in Case I
470 may have led to low hygroscopic growth of the aerosol mixture (especially for the coarse
471 mode). $f_{\beta}(80\%)$ values obtained (1.60 ± 0.03 for Case I and 3.00 ± 0.02 for Case II) are in
472 agreement with those presented in Titos et al., [2014a], that range between 1.4 and 3.4,
473 being larger in those cases with marine influence. $f_{\beta}(85\%)$ (2.10 ± 0.06 for Case I and $3.90 \pm$
474 0.03 for Case II) values are similar to those obtained in previous in-situ studies within
475 measurement differences limitations, ranging between 1.2 and 3.4 [Kim et al., 2006; Fierz-
476 Schmidhauser et al., 2010a,b; Adam et al., 2012; Zieger et al., 2013]. The γ values
477 obtained from the Hänel parameterization in these case studies are in the range of values
478 obtained in previous studies for the scattering coefficient using tandem of nephelometers
479 (between 0.1 and 1.35) [Raut and Chazette, 2007; Gasso et al., 2000; Randriamiarisoa et
480 al., 2006; Titos et al., 2014a,b].

481 The availability of the AERONET inversion retrieval data at late afternoon during
482 both cases as shown in Figure 1 allows us to retrieve volume concentration profiles by
483 means of LIRIC algorithm, assuming no drastic temporal change in aerosol properties

484 between the last AERONET retrieval and lidar measurements [Chaikovsky et al., 2008,
485 2012; Wagner et al., 2013; Granados-Muñoz et al., 2014]. Figure 6a represents these
486 volume concentration profiles obtained by the combination of lidar data from 20:30 to
487 21:00 UTC and the closest sun photometer retrieval (at 18:30 UTC) on Case I. Figure 6b
488 shows the volume concentration profiles for Case II retrieved from AERONET data at
489 18:10 UTC and lidar data from 20:00 to 20:30 UTC. As it can be observed, there is a
490 combination of coarse and fine particles along the whole profile for both cases. In both
491 cases, the fine mode volume concentration increases with altitude in both analysed layers.
492 The total volume concentration for Case I increases with height reaching a maximum
493 around 2500 m a.s.l. Figure 6c shows the volume concentration enhancement factor
494 ($f_{VC}(RH)$) for the fine mode and the total volume concentration against RH for Case I. In
495 this case, a threshold value of the volume concentration has been established at $10 \mu\text{m}^3/\text{cm}^3$
496 since $f_{VC}(RH)$ is a ratio and lower values may induce a significant overestimation of
497 $f_{VC}(RH)$. Because of this, RH_{ref} for the fine mode is around 73%. The fine mode volume
498 concentration presents a strong increase with RH, being $f_{VC}(80\%)=1.57$. The total volume
499 concentration smoothly increases with RH, mainly due to the increase in the fine mode
500 ($f_{VC}(80\%) = 1.16$ with $RH_{\text{ref}}=60\%$). For case II, Figure 7d shows $f_{VC}(RH)$ versus RH for the
501 fine mode and the total volume concentration. It is observed an increase of $f_{VC}(RH)$ with
502 RH for the fine mode, slightly smoother than in the previous case, with $f_{VC}(80\%) = 1.28$.
503 Using $RH_{\text{ref}}=60\%$ in order to make a comparison with Case I, $f_{VC}(80\%)$ for Case II is 1.57
504 which is larger than in Case I. According to these results, the fine mode is the one
505 dominating the hygroscopic growth in the analysed layers in both cases. Nonetheless, in
506 Case II there is a larger increase of the total volume concentration with RH than in Case I,
507 indicating that the coarse mode is more hygroscopic for Case II. This can be attributed to
508 the higher influence of the marine aerosol advected from the Mediterranean Sea in the
509 analysed layer in Case II and the minor influence of the residual mineral dust in the
510 analysed layer in Case I, evidencing the influence of the chemical composition on the
511 hygroscopic growth. Larger values of $f(RH)$ are usually obtained for fine mode particles [Di
512 Girolamo et al., 2012; Titos et al., 2014]. In our study, it seems that the fine mode is clearly
513 more dominated by more hygroscopic particles whereas the coarse mode is dominated by
514 substances with very low hygroscopic growth, especially for Case I (possible influence of

515 mineral dust in the aerosol mixture). Di Girolamo et al. [2012] observed similar behaviour
516 analysing aged dust particles partially mixed with maritime, urban and organic aerosols.
517 However, according to Zieger et al., [2013], the relative contribution of the fine and the
518 coarse modes and the specific chemical composition for each mode are very important for
519 determining $f(RH)$.

520 [Figure 6]

521 4. CONCLUSIONS

522 A new methodology to detect aerosol particle hygroscopic growth is implemented at
523 Granada EARLINET experimental site. Aerosol hygroscopic properties are analysed using
524 a multispectral lidar system in combination with radiosounding data obtained during
525 specific campaigns within the period 2011-2013. In the proposed method, an increase of the
526 aerosol particle backscatter coefficient with relative humidity is used to detect aerosol
527 hygroscopic growth. **In addition, results point out that there is an associated decrease in the
528 Angström exponent and in the particle depolarization ratio.** The hypothesis about the
529 positive correlation between the Angström exponent and the particle linear depolarization
530 ratio is presented here for the first time as an indicator of the aerosol hygroscopic growth.
531 **However, the decrease in the Angström exponent is not significant in the case studies
532 presented here since the variation is within the uncertainty limits. A further analysis with
533 additional and more reliable data (e. g. Raman measurements) is needed in order to
534 corroborate this hypothesis.**

535 The height independency of the air masses arriving at the station and of the water
536 vapour mixing ratio and the potential temperature profiles are also used as constraints in the
537 method presented here in order to provide more strictness to the identification of the
538 hygroscopic growth cases. The method proved to be reliable for the identification and
539 analysis of hygroscopic growth situations based on the analysis of the aerosol particle
540 properties profiles. The methodology is also applied to the analysis of the hygroscopic
541 growth effects on the volume concentration profiles retrieved by means of LIRIC
542 algorithm, which have never been done before.

543 Two cases of hygroscopic growth within the available dataset (one on 22nd July 2011
544 and another on 22nd July 2013) are presented in this study to illustrate the potential of the

545 exposed methodology. Different conditions were observed in these two cases allowing us to
546 analyse the hygroscopic behaviour of different aerosol types. In order to compare the two
547 analysed cases, the Hänel parameterization was used and data were recalculated using a
548 common RH_{ref} value of 40%. From this comparison, it was observed that the atmospheric
549 aerosol presented a stronger hygroscopic growth during the case study corresponding to
550 22nd July 2013, as indicated by $f_{\beta}(80\%)$, $f_{\beta}(85\%)$ and γ values. This can be explained by the
551 different atmospheric conditions in the two cases. The case corresponding to the 22nd July
552 2011 was affected by a mixture of atmospheric aerosols dominated by anthropogenic
553 pollution and slightly affected by mineral dust and marine aerosol, whereas the case
554 detected on 22nd July 2013 was influenced mainly by sulphates with a stronger influence of
555 marine aerosol than Case I, as indicated by AERONET data and the NAAPS model. The
556 values obtained for the backscatter enhancement factor $f_{\beta}(85\%)$, **considering the**
557 **associated uncertainties**, are within the range obtained with in-situ studies for the case on
558 22nd July 2011, and slightly larger on 22nd July 2013. **Uncertainties presented here are**
559 **related only to the aerosol backscatter coefficient. Since the experimental determination of**
560 **the enhancement factor by both remote sensing and in-situ instrumentation is not**
561 **straightforward and presents similar problems regarding its determination, further studies**
562 **should point in this direction and would be a significant contribution to this research field.**

563 The analysis of the volume concentration profiles reveals an increase of the total
564 volume concentration with relative humidity, dominated in our particular cases by an
565 increase in the fine mode fraction. The increase in the total volume concentration is larger
566 in Case II corresponding to the 22nd July 2013, due to the larger influence of the marine
567 aerosol for this case and to the slight influence of mineral dust (non hygroscopic particles)
568 on Case I.

569 ACKNOWLEDGEMENTS

570 This work was supported by the Andalusia Regional Government through projects
571 P12-RNM-2409 and P10-RNM-6299, by the Spanish Ministry of Science and Technology
572 through projects CGL2010-18782, and CGL2013-45410-R; by the EU through ACTRIS
573 project (EU INFRA-2010-1.1.16-262254); and by the University of Granada through the
574 contract “Plan Propio. Programa 9. Convocatoria 2013”. CIMEL Calibration was

575 performed at the AERONET-EUROPE calibration center, supported by ACTRIS
576 (European Union Seventh Framework Program (FP7/2007-2013) under grant agreement no.
577 262254. Granados-Muñoz was funded under grant AP2009-0552. The authors thankfully
578 acknowledge the computer resources, technical expertise, and assistance provided by the
579 Barcelona Supercomputing Center for the BSC-DREAM8b model dust data. The authors
580 express gratitude to the NOAA Air Resources Laboratory for the HYSPLIT transport and
581 dispersion model. We also thank those at the NRL-Monterey that helped in the
582 development of the NAAPS model.

583 REFERENCES

- 584 Alados-Arboledas, L., D. Müller, J. L. Guerrero-Rascado, F. Navas-Guzmán, D. Pérez-Ramírez,
585 and F. J. Olmo, Optical and microphysical properties of fresh biomass burning aerosol retrieved by
586 Raman lidar, and star- and sun-photometry, *Geophys. Res. Lett.*, 38, doi:10.1029/2010GL045999,
587 2011.
- 588 Adam, M., Putaud, J. P., Martins dos Santos, S., Dell'Acqua, A., and Gruening, C.: Aerosol
589 hygroscopicity at a regional background site (Ispra) in Northern Italy, *Atmos. Chem. Phys.*, 12(13),
590 5703-5717, 2012.
- 591 Bravo-Aranda, J. A., Navas-Guzmán, F., Guerrero-Rascado, J. L., Pérez-Ramírez, D., Granados-
592 Muñoz, M. J., and Alados-Arboledas, L., Analysis of lidar depolarization calibration procedure and
593 application to the atmospheric aerosol characterization, *Int. J. Remote. Sens.* 34(9-10), 3543-3560,
594 2013.
- 595 Chaikovsky, A., O. Dubovik, P. Goloub, N. Balashevich, A. Lopatsin, Y. Karol, S. Denisov, and T.
596 Lapyonok, Software package for the retrieval of aerosol microphysical properties in the vertical
597 column using combined lidar/photometer data (test version), Tech. Rep., Institute of Physics,
598 National Academy of Sciences of Belarus, Minsk, Belarus, 2008.
- 599 Chaikovsky, A., O. Dubovik, P. Goloub, D. Tanre, and G. Pappalardo, Wandinger, U.,
600 Chaikovskaya, L., Denisov, S., Grudo, Y., Lopatsin, A., Karol, Y., Lapyonok, T., Korol, M.,
601 Osipenko, F., Savitski, D., Slesar, A., Apituley, A., Arboledas, L. A., Biniotoglou, I., Kokkalis, P.,
602 Granados Muñoz, M. J., Papayannis, A., Perrone, M. R., Pietruczuk, A., Pisani, G., Rocadenbosch,
603 F., Sicard, M., De Tomasi, F., Wagner, J., and Wang, X., Algorithm and software for the retrieval
604 of vertical aerosol properties using combined lidar/radiometer data: Dissemination in EARLINET,,
605 paper presented at 26th International Laser and Radar Conference, Porto Heli, Greece, 2012.
- 606 Charlson, R. J., Schwartz, S. E., Hales, J. M., Cess, R. D. , Coakley Jr, J. A., Hansen, J. E., and
607 Hofmann, D. J., Climate forcing by anthropogenic aerosols, *Science*, 255(5043), 423-430, 1992.
- 608 Christensen, J. H., The Danish Eulerian hemispheric model—A three-dimensional air pollution
609 model used for the Arctic, *Atmos. Environ.*, 31(24), 4169-4191, 1997.
- 610 Covert, D. S., R. J. Charlson, and N. C. Ahlquist, A study of the relationship of chemical
611 composition and humidity to light scattering by aerosols, *J. Appl. Meteorol.*, 11, 968-976, 1972.
- 612 Di Girolamo, P., D. Summa, R. Bhawar, T. Di Iorio, M. Cacciani, I. Veselovskii, O. Dubovik, and
613 A. Kolgotin, Raman lidar observations of a Saharan dust outbreak event: characterization of the
614 dust optical properties and determination of particle size and microphysical parameters, *Atmos.*
615 *Environ.*, 50, 66-78, 2012.

616 Draxler, R. R., and G. D. Rolph, HYSPLIT (HYbrid Single-Particle Lagrangian Integrated
617 Trajectory) model access via NOAA ARL READY website (<http://www.arl.noaa.gov/ready/hysplit4.html>). NOAA Air Resources Laboratory, Silver Spring, edited, Md., 2003.
618

619 Dubovik, O., and M. D. King, A flexible inversion algorithm for retrieval of aerosol optical
620 properties from Sun and sky radiance measurements, *J. Geophys. Res.*, 105, 20,673–20,696,
621 doi:10.1029/2000JD900282, 2000.

622 Dubovik, O., B. Holben, T. F. Eck, A. Smirnov, Y. J. Kaufman, M. D. King, D. Tanré, and I.
623 Slutsker, Variability of absorption and optical properties of key aerosol types observed in
624 worldwide locations, *J. Atmos. Sci.*, 59(3), 590-608, 2002.

625 Dubovik, O., A. Sinyuk, T. Lapyonok, B. N. Holben, M. Mishchenko, P. Yang, T. F. Eck, H.
626 Volten, O. Muñoz, and B. Veihelmann, Application of spheroid models to account for aerosol
627 particle nonsphericity in remote sensing of desert dust, *J. Geophys. Res-Atmos.*, (1984–2012),
628 111(D11), 2006.

629 Eck, T. F., B. N. Holben, J. S. Reid, O. Dubovik, A. Smirnov, N. T. O'Neill, I. Slutsker, and S.
630 Kinne, Wavelength dependence of the optical depth of biomass burning, urban, and desert dust
631 aerosols, *J. Geophys. Res-Atmos.*, (1984–2012), 104(D24), 31333-31349, 1999.

632 Feingold, G., and B. Morley, Aerosol hygroscopic properties as measured by lidar and comparison
633 with in situ measurements, *Journal of geophysical research*, 108(D11), 4327, 2003.

634 Feingold, G., R. Furrer, P. Pilewskie, L. A. Remer, Q. Min, and H. Jonsson, Aerosol indirect effect
635 studies at Southern Great Plains during the May 2003 intensive operations period, *J. Geophys. Res.*,
636 111(D5), D05S14, 2006.

637 Fernald, F. G., Analysis of atmospheric lidar observations- Some comments, *Applied Optics*, 23(5),
638 652-653, 1984.

639 Fernald, F. G., B. M. Herman, and J. A. Reagan, Determination of aerosol height distributions by
640 lidar, *J. Appl. Meteorol.*, 11(3), 482-489, 1972.

641 Ferrare, R. A., S. H. Melfi, D. N. Whiteman, K. D. Evans, M. Poellot, and Y. J. Kaufman, Raman
642 lidar measurements of aerosol extinction and backscattering: 2. Derivation of aerosol real refractive
643 index, single- scattering albedo, and humidification factor using Raman lidar and aircraft size
644 distribution measurements, *J. Geophys. Res-Atmos.*, (1984–2012), 103(D16), 19673-19689, 1998.

645 Fierz-Schmidhauser, R., P. Zieger, G. Wehrle, A. Jefferson, J. A. Ogren, U. Baltensperger, and E.
646 Weingartner, Measurement of relative humidity dependent light scattering of aerosols. *Atmos.*
647 *Meas. Tech.*, 3, 39-50, 2010a.

648 Fierz-Schmidhauser, R., P. Zieger, M. Gysel, L. Kammermann, P. F. DeCarlo, U. Baltensperger,
649 and E. Weingartner, Measured and predicted aerosol light scattering enhancement factors at the
650 high alpine site Jungfraujoch, *Atmos. Chem. Phys.*, 10(5), 2319-2333, 2010b.

651 Franke, K., et al. (2001), One-year observations of particle lidar ratio over the tropical Indian Ocean
652 with Raman lidar, *Geophysical Research Letters*, 56, 1766{1782, doi: 10.1029/2001GL013671.

653 Gasso, S., D. A. Hegg, D. S. Covert, D. Collins, K. J. Noone, E. Öström, B. Schmid, P. B. Russell,
654 J. M. Livingston, and P. A. Durkee, Influence of humidity on the aerosol scattering coefficient and
655 its effect on the upwelling radiance during ACE- 2, *Tellus B*, 52(2), 546-567, 2000.

656 Granados-Muñoz, M.J., Navas-Guzmán, F., Bravo-Aranda, J.A., Guerrero-Rascado, J.L., Lyamani,
657 H., Fernández-Gálvez, J., and Alados-Arboledas, L., Automatic determination of the planetary
658 boundary layer height using lidar: one-year analysis over southeastern Spain. *J. Geophys. Res-*
659 *Atmos.*, 117, D18208. <http://dx.doi.org/10.1029/2012JD017524>, 2012.

660 Granados-Muñoz, M. J., Guerrero-Rascado, J. L., Bravo-Aranda, J. A., Navas-Guzmán, F.,
661 Valenzuela, A., Lyamani, H., Chaikovsky, A., Wandinger, U., Ansmann, A. Dubovik, O., Grudo, J.
662 O. and Alados-Arboledas, L., Retrieving aerosol microphysical properties by Lidar- Radiometer
663 Inversion Code (LIRIC) for different aerosol types. *J. Geophys. Res-Atmos.*, 119(8), 4836-4858,
664 2014.

665 Guerrero-Rascado, J. L., Ruiz, B., and Alados-Arboledas, L., Multi-spectral Lidar characterization
666 of the vertical structure of Saharan dust aerosol over southern Spain. *Atmos. Environ.*, 42(11),
667 2668-2681, 2008.

668 Guerrero-Rascado, J. L., F. J. Olmo, I. Avilés-Rodríguez, F. Navas-Guzmán, D. Pérez-Ramírez, H.
669 Lyamani, and L. Alados-Arboledas, Extreme Saharan dust event over the southern Iberian
670 Peninsula in September 2007: Active and passive remote sensing from surface and satellite, *Atmos.*
671 *Chem. Phys.*, 9(21), 8453-8469, 2009.

672 Guerrero-Rascado, J. L., Andrey, J., Sicard, M., Molero, F., Comerón, A., Pujadas, M., ... &
673 Alados-Arboledas, L., Aerosol closure study by lidar, Sun photometry, and airborne optical
674 counters during DAMOCLES field campaign at El Arenosillo sounding station, Spain. *J. Geophys.*
675 *Res-Atmos.*, (1984–2012), 116(D2), 2011.

676 Hänel, G., The Properties of Atmospheric Aerosol Particles as Functions of the Relative Humidity
677 at Thermodynamic Equilibrium with the Surrounding Moist Air, in *Advances in Geophysics*, edited
678 by H. E. Landsberg and J. V. Mieghem, pp. 73-188, Elsevier, 1976.

679 Hegg, D. A., D. S. Covert, M. J. Rood, and P. V. Hobbs, Measurements of aerosol optical properties
680 in marine air, *J. Geophys. Res-Atmos.*, (1984–2012), 101(D8), 12893-12903, 1996.

681 Holben, B. N., et al., AERONET—A Federated Instrument Network and Data Archive for Aerosol
682 Characterization, *Remote Sensing of Environment*, 66(1), 1-16, 1998.

683 IPCC, Contribution of Working Group I to the Fifth Assessment Report of the Intergovernmental
684 Panel on Climate Change, in *Summary for Policymakers in Climate Change*, edited by T. F.
685 Stocker, D. Qin, G.K. Plattner, M. Tignor, S. Allen, J. Boschung, A. Nauels, Y. Xia, V. Bex, and P.
686 Midgley, Cambridge University Press, 2013.

687 Kim, J., Yoon, S. C., Jefferson, A., and Kim, S. W., Aerosol hygroscopic properties during Asian
688 dust, pollution, and biomass burning episodes at Gosan, Korea in April 2001. *Atmos. Environ.*,
689 40(8), 1550-1560, 2006.

690 Klett, J. D., Stable analytical inversion solution for processing lidar returns, *Applied Optics*, 20(2),
691 211-220, 1981.

692 Klett, J. D. (1985), Lidar inversion with variable backscatter/extinction ratios, *Applied Optics*,
693 24(11), 1638-1643.

694 Kovalev, V. A. (1995). Sensitivity of the Lidar Solution to Errors of the Aerosol Backscatter-to-
695 Extinction Ratio - Influence of a Monotonic Change in the Aerosol Extinction Coefficient. *Applied*
696 *Optics*, 34(18), 3457-3462.

697 Kovalev, V. A. and W. E. Eichinger (2004). *Elastic Lidar: Theory, Practice, and Analysis Methods*,
698 Wiley.

699 Landulfo, E., Papayannis, A., Artaxo, P., Castanho, A. D. A., De Freitas, A. Z., Souza, R. F. and
700 Moreira, D. S., Synergetic measurements of aerosols over Sao Paulo, Brazil using LIDAR,
701 sunphotometer and satellite data during the dry season. *Atmos. Chem. Phys.*, 3(5), 1523-
702 1539, 2003.

703 Lyamani, H., Olmo, F. J., Alcántara, A., & Alados-Arboledas, L., Atmospheric aerosols during the
704 2003 heat wave in southeastern Spain I: Spectral optical depth. *Atmos. Environ.*, 40(33), 6453-
705 6464, 2006.

706 Lyamani, H., Olmo, F. J., Alcántara, A., & Alados-Arboledas, L., Atmospheric aerosols during the
707 2003 heat wave in southeastern Spain II: microphysical columnar properties and radiative forcing.
708 *Atmos. Environ.*, 40(33), 6465-6476, 2006.

709 Massling, A., Leinert, S., Wiedensohler, A. and Covert., D., Hygroscopic growth of sub-micrometer
710 and one-micrometer aerosol particles measured during ACE-Asia. *Atmos. Chem. Phys.*, 7, 3249-
711 3259, doi:10.5194/acp-7-3249-2007, 2007.

712 Navas-Guzmán, F., Fernández-Gálvez, J., Granados-Muñoz, M. J., Guerrero-Rascado, J. L., Bravo-
713 Aranda, J. A., and Alados-Arboledas, L., Tropospheric water vapour and relative humidity profiles
714 from lidar and microwave radiometry. *Atmos. Meas. Tech.*, 7(5), 1201-1211, 2014.

715 Navas-Guzmán, F., Bravo-Aranda, J. A., Guerrero-Rascado, J. L., Granados-Muñoz, M. J., and
716 Alados-Arboledas, L., Statistical analysis of aerosol optical properties retrieved by Raman lidar
717 over Southeastern Spain. *Tellus B*, 65, 2013.

718 O'Neill, N. T., T. F. Eck, A. Smirnov, B. N. Holben, and S. Thulasirama, Spectral discrimination of
719 coarse and fine mode optical depth, *J. Geophys. Res.*, 108(D17), 4559, 2003.

720 Padró, L. T., D. Tkacik, T. Latham, C. J. Hennigan, A. P. Sullivan, R. J. Weber, L. G. Huey, and A.
721 Nenes, Investigation of cloud condensation nuclei properties and droplet growth kinetics of the
722 water-soluble aerosol fraction in Mexico City, *J. Geophys. Res.*, 115, D09204,
723 doi:10.1029/2009JD013195, 2010.

724 Pahlow, M., Feingold, G., Jefferson, A., Andrews, E., Ogren, J. A., Wang, J. and Turner, D. D.,
725 Comparison between lidar and nephelometer measurements of aerosol hygroscopicity at the
726 Southern Great Plains Atmospheric Radiation Measurement site. *J. Geophys. Res-Atmos.*, (1984-
727 2012), 111(D5), 2006.

728 Pappalardo, G., et al., Aerosol lidar intercomparison in the framework of the EARLINET project. 3.
729 Raman lidar algorithm for aerosol extinction, backscatter, and lidar ratio, *Appl. Opt.*, 43 , 5370-
730 5385, 2004.

731 Pappalardo, G., Amodeo, A., Apituley, A., Comeron, A., Freudenthaler, V., Linné, H., Ansmann,
732 A., Bösenberg, J., D'Amico, G., Mattis, I., Mona, L., Wandinger, U., Amiridis, V., Alados-
733 Arboledas, L., Nicolae, D., and Wiegner, M., EARLINET: towards an advanced sustainable
734 European aerosol lidar network, *Atmos. Meas. Tech. Discuss.*, 7, 2929-2980, doi: 10.5194/amtd-7-
735 2929-2014, 2014.

736 Preissler, J., F. Wagner, S. N. Pereira, and J. L. Guerrero-Rascado (2011a), Multiinstrumental
737 observation of an exceptionally strong Saharan dust outbreak over Portugal, *Journal of Geophysical*
738 *Research*, 116, D24,204, doi:10.1029/2011JD016527.

739 Randriamiarisoa, H., Chazette, P., Couvert, P., Sanak, J. and Mégie, G., Relative humidity impact
740 on aerosol parameters in a Paris suburban area, *Atmos. Chem. Phys.*, 6(5), 1389-1407, 2006.

741 Raut, J. C., and P. Chazette, Retrieval of aerosol complex refractive index from a synergy between
742 lidar, sunphotometer and in situ measurements during LISAIR experiment, *Atmos. Chem. Phys.*,
743 7(11), 2797-2815, 2007.

744 Stull, R. B. (1988), *An Introduction to Boundary Layer Meteorology*, Kluwer Acad., Dordrecht,
745 Netherlands.

746 Stunder, B.J.B., An assessment of the quality of forecast trajectories. *J. Appl. Meteorol.*, , 35, 1319-
747 1331, 1996.

748 Sun, B., Reale, A., Schroeder, S., Seidel, D. J., and Ballish, B. Toward improved corrections
749 for radiation-induced biases in radiosonde temperature observations. *J. Geophys. Res-*
750 *Atmos.*, 118(10), 4231-4243, 2013.

751 Titos, G., Foyo-Moreno, I., Lyamani, H., Querol, X., Alastuey, A., and Alados-Arboledas, L.,
752 Optical properties and chemical composition of aerosol particles at an urban location: An estimation
753 of the aerosol mass scattering and absorption efficiencies. *J. Geophys. Res-Atmos.*, (1984–2012),
754 117(D4), 2012.

755 Titos, G., Jefferson, A., Sheridan, P. J., Andrews, E., Lyamani, H., Alados-Arboledas, L., & Ogren,
756 J. A. , Aerosol light-scattering enhancement due to water uptake during TCAP campaign. *Atmos.*
757 *Chem. Phys.*, 14, 7031–7043, 2014a.

758 Titos, G., H. Lyamani, M. Pandolfi, A. Alastuey, and L. Alados-Arboledas, Identification of fine
759 (PM1) and coarse (PM10-1) sources of particulate matter in an urban environment. *Atmos.*
760 *Environ.*, 89, 593-602, 2014b.

761 Titos, G., H. Lyamani, A. Cazorla, M. Sorribas, I. Foyo-Moreno, A. Wiedensohler and L. Alados-
762 Arboledas, Study of the relative humidity dependence of aerosol light-scattering in southern Spain.
763 Under review for publication in *TellusB*, 2014c.

764 Valenzuela, A., F. J. Olmo, H. Lyamani, M. Antón, A. Quirantes, and L. Alados-Arboledas,
765 Classification of aerosol radiative properties during African desert dust intrusions over southeastern
766 Spain by sector origins and cluster analysis, *J. Geophys. Res-Atmos.*, (1984–2012), 117(D6), 2012.

767 Veselovskii, I., D. N. Whiteman, A. Kolgotin, E. Andrews, and M. Korenskii, Demonstration of
768 aerosol property profiling by multiwavelength lidar under varying relative humidity conditions, *J.*
769 *Atmos. Ocean. Tech.*, 26(8), 1543-1557, 2009.

770 Wagner, J., A. Ansmann, U. Wandinger, P. Seifert, A. Schwarz, M. Tesche, A. Chaikovsky, and O.
771 Dubovik, Evaluation of the Lidar/Radiometer Inversion Code (LIRIC) to determine microphysical
772 properties of volcanic and desert dust, *Atmos. Meas. Tech.*, 6(7), 1707-1724, 2013.

773 Wu, A., W. Birmili, L. Poulain, Z. Wang, M. Merkel, B. Fahlbusch, D. van Pinxteren, H.
774 Herrmann, and A. Wiedensohler, Particle hygroscopicity during atmospheric new particle formation
775 events: implications for the chemical species contributing to particle growth. *Atmos. Chem. Phys.*,
776 13, 6637-6646, 2013.

777 Wulfmeyer, V., and G. Feingold, On the relationship between relative humidity and particle
778 backscattering coefficient in the marine boundary layer determined with differential absorption
779 lidar, *J. Geophys. Res-Atmos.*, (1984–2012), 105(D4), 4729-4741, 2000.

780 Zieger, P., Fierz-Schmidhauser, R., Weingartner, E., and Baltensperger, U., Effects of relative
781 humidity on aerosol light scattering: results from different European sites. *Atmos. Chem. Phys.*,
782 13(21), 10609-10631, 2013.

783

784

785

786

787

788

789
790
791
792
793
794
795
796

	Case I		Case II	
	1330 m a.s.l.	2330 m a.s.l	1300 m a.s.l.	2700 m a.s.l.
$\beta_{532\text{nm}}^{\text{aer}} (\text{Mm}^{-1}\cdot\text{sr}^{-1})$	2.17	4.20	1.11	3.84
RH (%)	60	90	40	85
$\beta\text{-AE}(355\text{-}532\text{nm})$	1.3	0.8	2.0	1.0
$\delta_{532\text{nm}}^{\text{P}}$	0.10	0.05	0.07	0.03

797 Table 1. Values of the different aerosol properties at the lowest and highest altitudes of the analysed layers for
798 Case I and Case II.

799
800
801
802
803
804
805
806
807
808

809
810
811
812
813
814
815
816

	Case I	Case II
$f_{\beta}(80\%)$	1.6 ± 0.6	3.0 ± 1.0
γ	0.56 ± 0.22	1.1 ± 0.4
$f_{\beta}(85\%)$	2.1 ± 0.8	3.9 ± 1.5

817 Table 2. Values of $f_{\beta}(80\%)$, $f_{\beta}(85\%)$ and γ for the two cases of hygroscopic growth corresponding to the
818 22nd July of 2011 and 2013, respectively. The uncertainties in $f_{\beta}(RH)$ are obtained by error propagation
819 applied to Eq. 1. Only the uncertainty introduced by the aerosol particle backscatter coefficient is
820 considered.

821
822
823
824
825
826
827
828
829
830
831
832

833

834

835

836

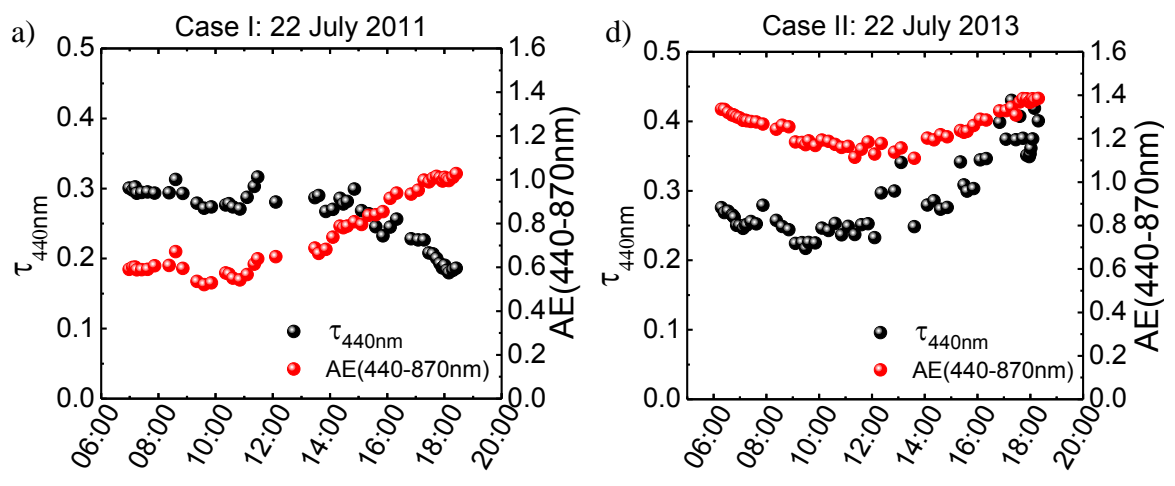
837

838

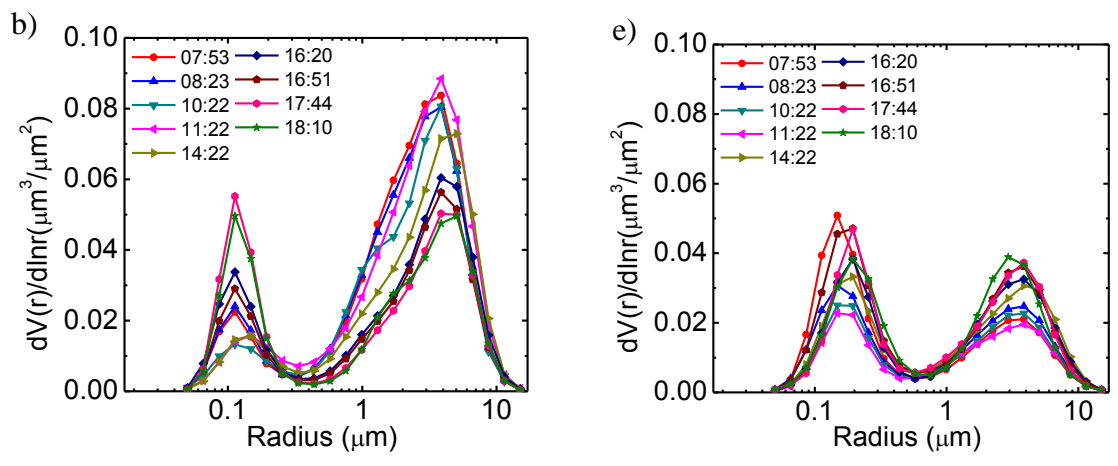
839

840 Figures:

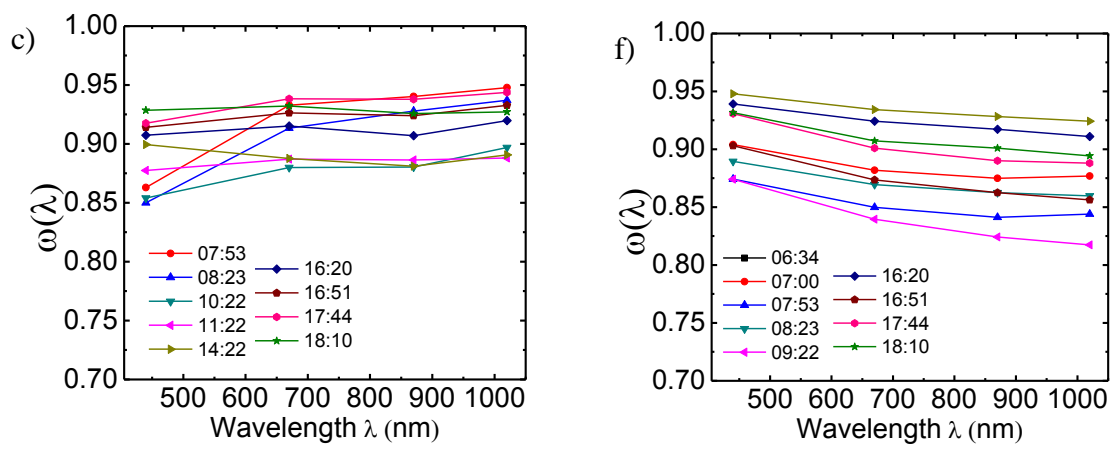
841



842

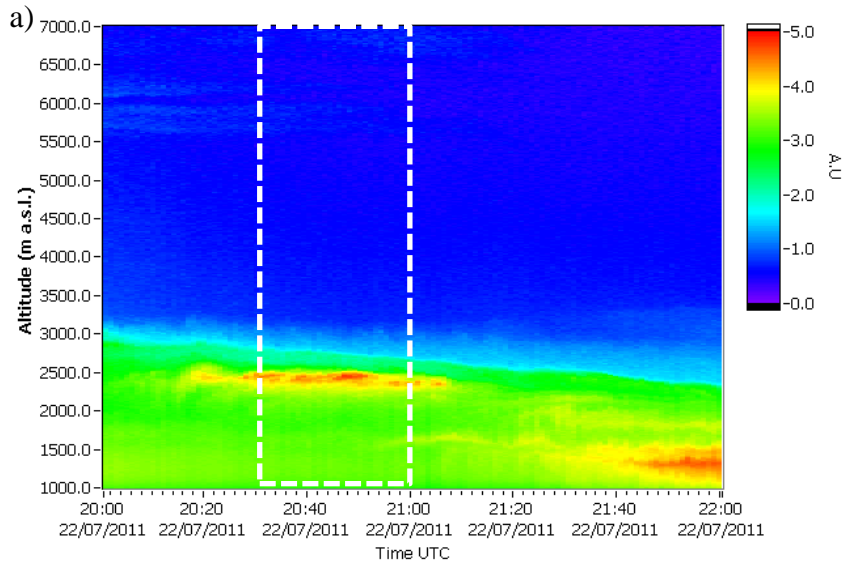


843

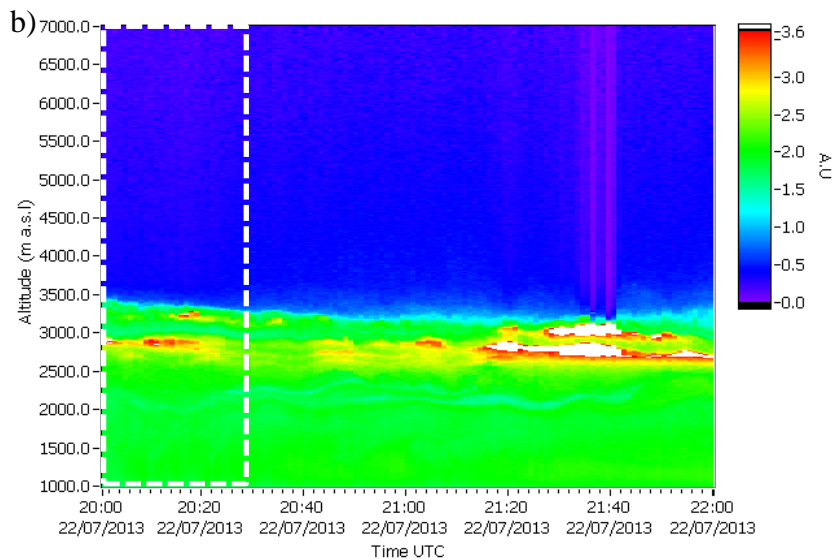


844

845 Figure 1. a) AERONET τ_{440} and AE(440-870) daily time series for Case I. b) AERONET retrieved volume
 846 size distributions for Case I. c) $\omega(\lambda)$ for Case I. d) AERONET τ_{440} and AE(440-870) daily time series for
 847 Case II. e) AERONET retrieved volume size distributions for Case II. f) $\omega(\lambda)$ for Case II.



848



849

850

851 Figure 2. a) Lidar RCS time series at 532 nm (arbitrary units) on 22nd July 2011 from 20:00 to 22:00
 852 UTC. **Features shown here are aerosol related.** b) Lidar RCS time series at 532 nm (arbitrary units) on
 853 22th July 2013 from 20:00 to 22:00 UTC. **For this case, some clouds were present between 21:35-24:45,**
 854 **leading to a strong attenuation of the RCS. On both cases data were cloud-screened before proceeding**
 855 **to the investigation of hygroscopic growth effects.**

856

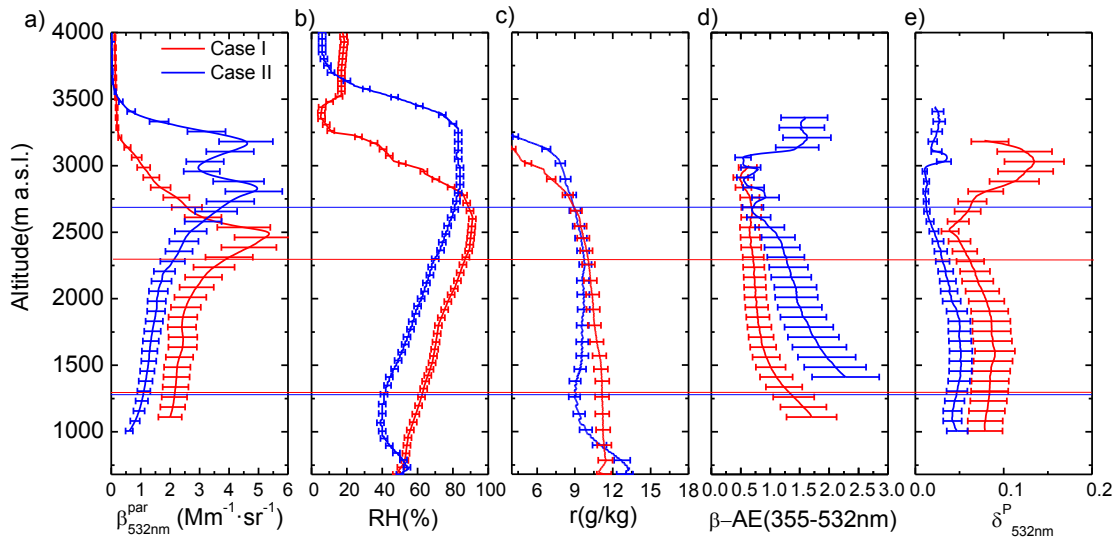
857

858

859

860

861



862

863

864 Figure 3. a) $\beta^{\text{P}}_{532\text{nm}}$ retrieved with Klett-Fernald algorithm (LR=65 sr for Case I and LR=70 for Case II)
 865 from 20:30 to 21:00 UTC on Case I and 20:00 to 20:30 UTC on Case II b) RH profiles from the
 866 radiosounding launched at 20:30 UTC on Case I and at 20:00 UTC on Case II. c) r profiles from the
 867 radiosounding launched at 20:30 UTC on Case I and at 20:00 UTC on Case II. d) $\beta\text{-AE}(355\text{-}532\text{nm})$
 868 retrieved with Klett-Fernald algorithm for the same periods. e) $\delta^{\text{P}}_{532\text{nm}}$ retrieved from lidar data for the
 869 same periods. Horizontal lines represent the height limits of the aerosol layers selected for the analysis
 870 in Case I (red line) and Case II (blue lines).

871

872

873

874

875

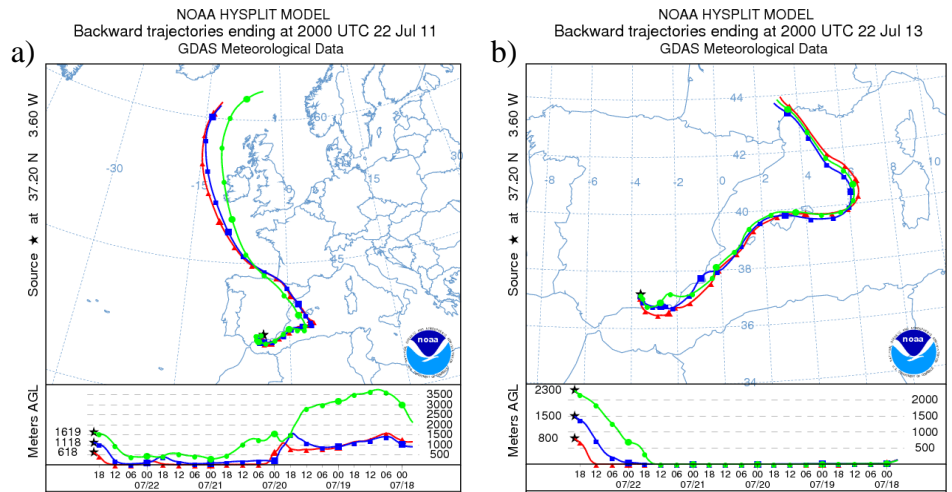
876

877

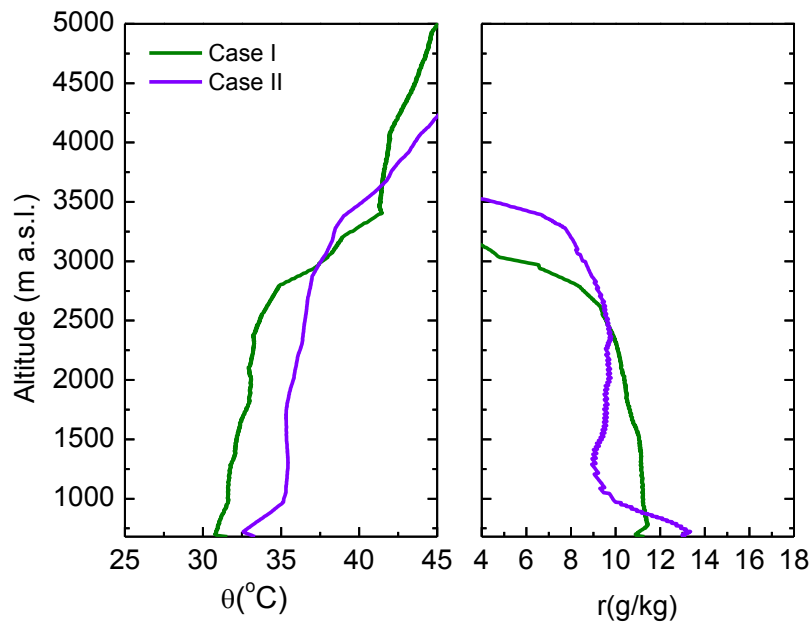
878

879

880



c)



881

882

883

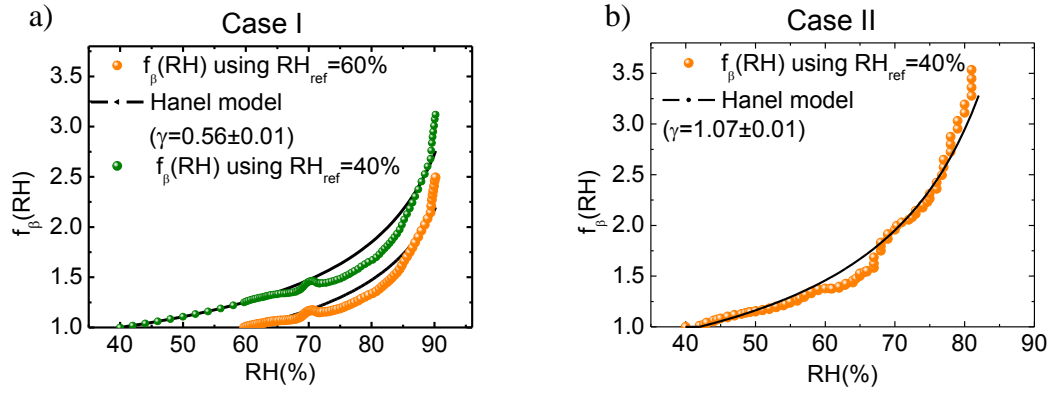
884

885

886 Figure 4. a) 5-day backtrajectories of the air masses ending on 22nd July 2011 at 20:00 at Granada at 3
887 altitude heights within 1330-2330 m a.s.l. height range. b) 5-day backtrajectories of the air masses
888 ending on 22nd July 2013 at 20:00 at Granada at 3 altitude heights within 1300-2700 m a.s.l. height
889 range. c) Vertical profiles of θ (in $^{\circ}\text{C}$) and r (in g/kg) from radiosounding data on 22nd July 2011 at
890 20:30 UTC (Case I) and 22nd July 2013 at 20:00 UTC (Case II).

891

892

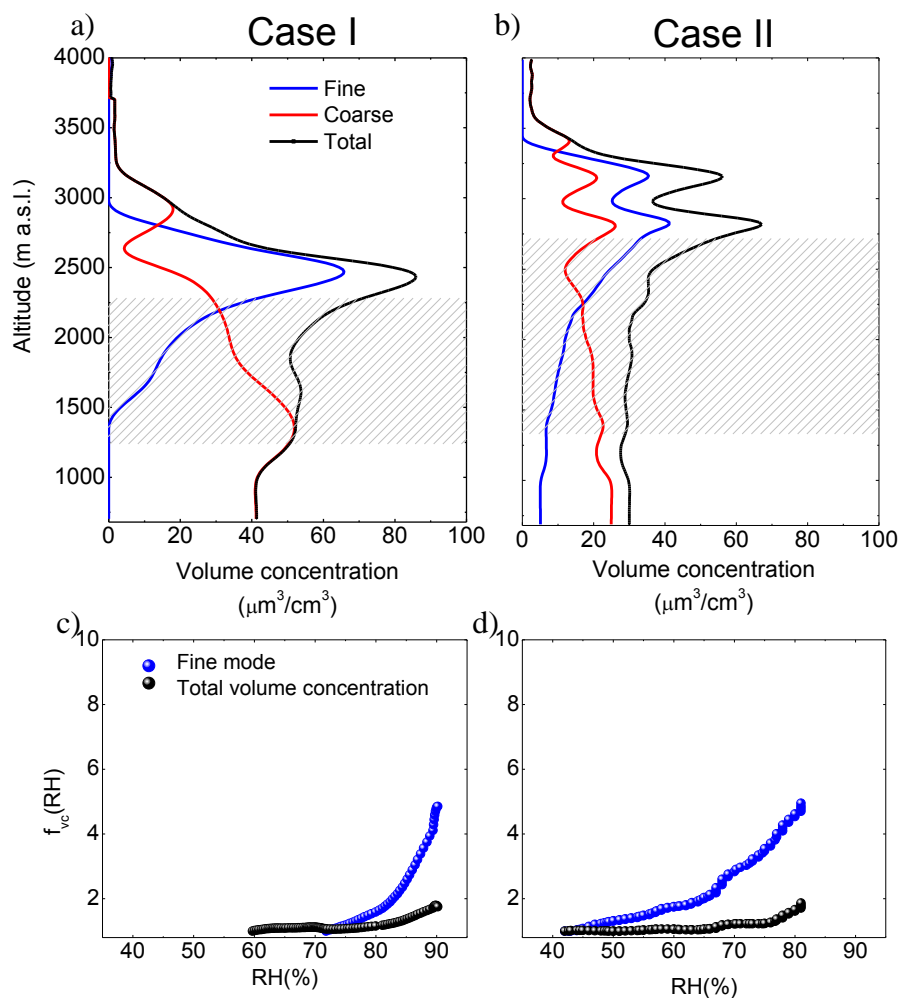


893

894

895 Figure 5. a) $f_{\beta}(RH)$ retrieved on 22nd July 2011 (Case I) from 20:30 to 21:00 UTC for the height range
 896 between 1330 and 2330 m a.s.l. (yellow dots for $RH_{ref}=60\%$ and green dots for $RH_{ref}=40\%$). b) $f_{\beta}(RH)$
 897 retrieved on 22nd July 2013 (Case II) from 20:00 to 20:30 UTC for the layer corresponding to heights
 898 between 1300 and 2700 m a.s.l. using $RH_{ref}=40\%$.

899



900

901

902

903 Figure 6. a) LIRIC retrieved volume concentration (fine mode, coarse mode and total concentration)
 904 profiles on 22nd July 2011 from 20:30 to 21:00 UTC. The shaded area indicates the height range where
 905 hygroscopic growth was investigated. b) LIRIC retrieved volume concentration profiles on 22nd July
 906 2013 from 20:00 to 20:30 UTC. The shaded area indicates the investigated height range. c) $f_{vc}(RH)$
 907 versus RH for the fine mode and the total volume concentrations for 22nd July 2011 and the layer
 908 corresponding to heights between 1330 and 2330 m a.s.l. d) $f_{vc}(RH)$ versus RH for the fine mode and
 909 the total volume concentrations for 22nd July 2013 and the layer corresponding to heights between
 910 1300 and 2700 m a.s.l.